



Trans. Nonferrous Met. Soc. China 34(2024) 3295-3308

ScienceDirect
Nonferrous Metals
Society of China

www.tnmsc.cn

Transactions of



Enhanced mechanical properties of molybdenum alloy originating from

composite strengthening of Re and CeO₂

Meng-yao ZHANG¹, Shuai MA¹, Xin LI¹, Ye GAO¹, Zhuang-zhi WU^{1,2}, De-zhi WANG^{1,2}

- 1. School of Materials Science and Engineering, Central South University, Changsha 410083, China;
- 2. State Key Laboratory of Powder Metallurgy, Central South University, Changsha 410083, China

Received 30 June 2024; accepted 12 September 2024

Abstract: To enhance the mechanical properties of molybdenum alloys at both room and high temperatures, Mo-14Re-1CeO₂ alloy was synthesized using the powder metallurgy method, and the corresponding microstructure and mechanical properties were characterized. The results indicate that the ultimate tensile strength of Mo-14Re-1CeO₂ reaches 657 MPa, with a total elongation of 35.2%, significantly higher than those of pure molybdenum (453 MPa, and 7.01%). Furthermore, the compression strength of Mo-14Re-1CeO₂ at high temperature (1200 °C) achieves 355 MPa, which is still larger than that of pure molybdenum (221 MPa). It is revealed that there is a coherent interface between CeO₂ and the Mo-14Re matrix with CeO₂ particles uniformly distributed in both intergranular and intragranular regions. The improvements in mechanical properties are primarily attributed to the formation of Mo-Re solid solution, grain refinement, and dispersion strengthening effect of CeO₂.

Key words: molybdenum-rhenium alloy; cerium oxide; composite strengthening; mechanical properties

1 Introduction

Molybdenum (Mo) and its alloys recognized for their high-temperature strength, elevated melting point, minimal thermal expansion, and superior creep resistance ability, making them indispensable in a range of industrial applications, particularly in the aerospace and automotive fields [1,2]. However, the intrinsic brittleness limited ductility associated with temperature and deteriorated strength at high of Mo restrict its temperatures applications. To address these issues, extensive efforts have been dedicated to the improvement of mechanical properties of Mo alloys [3–6].

The most widely adopted methods include solid solution and dispersion strengthening [7].

Among the diverse elements that can be alloyed in solid solution to strengthen molybdenum, rhenium (Re) stands out for its exceptional strengthening efficacy. The incorporation of Re into Mo alloys elicits the "Rhenium effect" [8], mitigating the low-temperature brittleness characteristic molybdenum. This enhancement in ductility at low temperatures not only bolsters the machinability of the alloys but also permits an augmentation in strength without compromising their overall plasticity [9]. At the same time, "Rhenium effect" makes Mo-Re alloys take the potential to be excellent high-temperature structural materials [10]. Notably, when the rhenium content is optimized to approximately 14%, the molybdenum-rhenium alloy achieves an elongation of about 40%, indicating superior ductility [11].

Furthermore, rare earth metal oxides, such as

Corresponding author: Zhuang-zhi WU, Tel: +86-19198136866, E-mail: zwu@csu.edu.cn; De-zhi WANG, Tel: +86-13974945608, E-mail: dzwang@csu.edu.cn

DOI: 10.1016/S1003-6326(24)66609-4

1003-6326/© 2024 The Nonferrous Metals Society of China. Published by Elsevier Ltd & Science Press

lanthanum oxide (La₂O₃), yttrium oxide (Y₂O₃), and cerium oxide (CeO₂), are known for their high melting points, hardness, and thermal stability [12–15]. When uniformly dispersed in molybdenum as micro- or nano-sized particles, these oxides effectively deter the grain growth and substantially enhance the strength [16]. These specific rare earth oxides also provide strengthening effects for molybdenum-rhenium alloys [17]. The exploration of multi-element composite strengthening for high-performance molybdenum-based materials is ongoing [18]. MUELLER et al [17] observed that a dispersion-strengthened molybdenum alloy (La₂O₃-Mo) with an added requisite amount of Re exhibited a ductile-to-brittle transition temperature significantly below room temperature, increased tensile strength in the range of 1000-1250 °C. Similarly, LIU et al [19] reported that a Mo-Re-La alloy, prepared by doping with 0.6% (mass fraction) La₂O₃ particles, surpassed the mechanical properties of both pure Mo (P-Mo) and the Mo-Re alloys. Despite these advances, the integration of CeO₂ into Mo-Re alloys has not been reported.

Hence, in this work, the composite effect of Re and CeO₂ on the mechanical properties of Mo has been explored, and the corresponding underlying strengthening mechanism is also discussed to confirm the potential of alloy design and micro-structural control in advancing the applicative prospects of molybdenum alloys.

2 Experimental

2.1 Materials and preparation

The raw powders included molybdenum powder (99.9%, Shanghai Macklin Biochemical, China), rhenium powder (99.9%, Shanghai Macklin Biochemical, China), and CeO₂ powder (99.9%, Shanghai Macklin Biochemical, China), as depicted in Fig. 1. And the abbreviations and compositions of the diverse samples are demonstrated in Table 1.

Firstly, the raw powders, weighed according to specific mass percentages (Table 1), were mixed in a mixing bottle with a ball-to-powder mass ratio of 3:1 at 120 r/min for 12 h to ensure thorough homogeneity. Subsequently, the mixture was transferred to a mold (42 mm × 15 mm) and pressed at 260 MPa for 2 min. Then, the billets were sintered

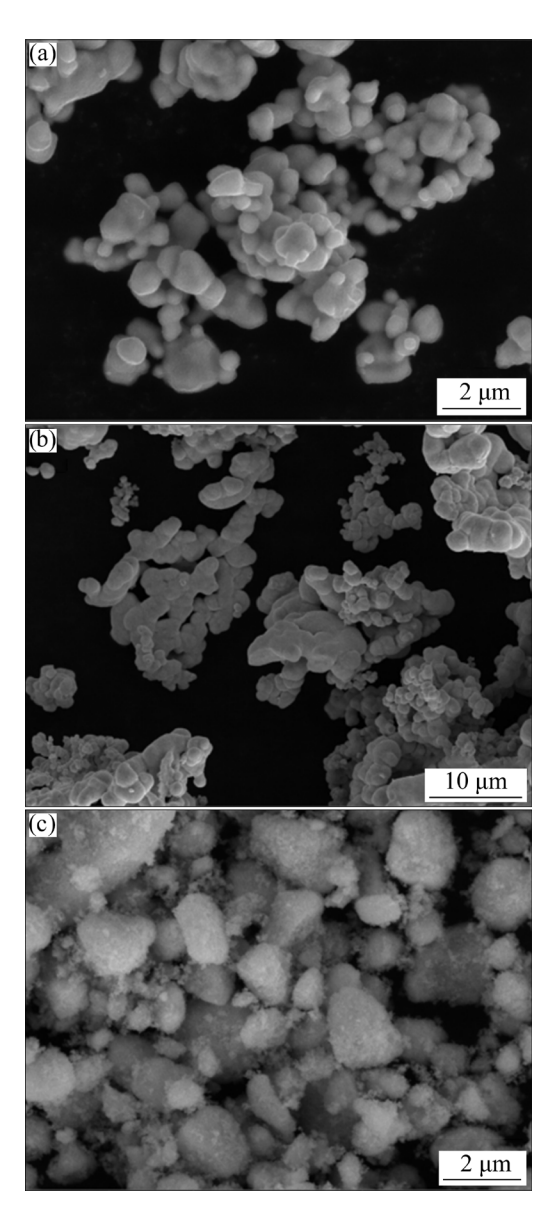


Fig. 1 SEM images of raw powders: (a) Mo; (b) Re; (c) CeO_2

Table 1 Chemical compositions of samples (wt.%)

Sample	CeO_2	Re	Mo
P-Mo	0	0	Bal.
Mo-14Re	0	14	Bal.
Mo-1CeO ₂	1	0	Bal.
Mo-14Re-1CeO ₂	1	14	Bal.

at 1900 °C for 2 h in a hydrogen atmosphere using a furnace (SWSL2000/15, Jujing, China). During sintering process, the temperature ramp rate was 10 °C/min up to 1000 °C, after which it was reduced to 8 °C/min. Finally, the samples were gradually cooled to room temperature with a rate of 10 °C/min.

2.2 Characterization

The phase composition of various samples was detected by a Rigaku TTR III X-ray diffractometer (MiniFlex600, Cu K_{α} radiation) from 20° to 80° with 5 (°)/min. The tensile mechanical properties were evaluated using an electronic universal testing machine (DDL300, Sinotest). To guarantee the precision of experimental results, each test was conducted thrice, and the results were reported as the mean of these trials. The tensile testing was conducted at room temperature with a crosshead speed of 0.6 mm/min. The dimension of the test samples could be found in the previous work [20]. The density was measured by a densitometer (DE-120 M, DahoMeter) according to the Archimedes principle. Additionally, the Vickers hardness was measured by a digital microhardness tester (HVS-1000, Lianer, Shanghai, China) with 1.0 kg for 10 s, taking the average of at least five indentation points. To investigate the mechanical properties of Mo alloys at 1200 °C, compression tests were executed with a strain rate of 0.1 s⁻¹ on Gleeble-3180. The specimens for the compression tests, which were oriented normally to the extrusion direction, were 5 mm and 8 mm in diameter and height, respectively.

Scanning electron microscopy (SEM, Tescan MIRA4) equipped with energy dispersive spectroscopy (EDS) was employed to observe the morphology and analyze elemental distribution, and all the specimens should be pretreated by submerging in the reagent (20 mL aqueous solution of 2.6 g K₃Fe(CN)₆ and 2.3 g NaOH) for 3 min. The average grain size was calculated using the linear intercept method. The surface morphology of the metallographic samples with smooth surfaces and no damage was obtained using a scanning electron microscope, ensuring that the images were clear and the grain boundaries were visible. Then, the grain size was statistically evaluated with the help of image process software (Image-pro plus 6.0) and at least 200 random particles were measured. Transmission electron microscopy (TEM, Tecnai G2 F20) was used to observe the microstructures. For TEM analysis, the thin foils obtained from the samples were initially ground to a thickness of 60-80 µm. The final step of thinning and perforation was achieved using a twin-jet electropolishing technique, which was conducted in a solution of 10 vol.% perchloric acid in alcohol at −25 °C with an applied current of 90 mA.

3 Results

3.1 Phase and microstructures

Figure 2 displays the X-ray diffraction (XRD) patterns of sintered billets (Fig. 2(a)) with a magnified view focusing on the 2θ angle range from 39.6° to 41° (Fig. 2(b)). It is evident that in Mo–14Re and Mo–14Re–1CeO₂, the primary diffraction peaks of Mo shift towards higher angles, suggesting the formation of solid solution with reduced lattices due to a smaller atomic diameter of Re [21,22]. Specifically, Fig. 2(b) highlights the position of the main peak, and the peak is shifted to the right clearly, corroborating the previous results.

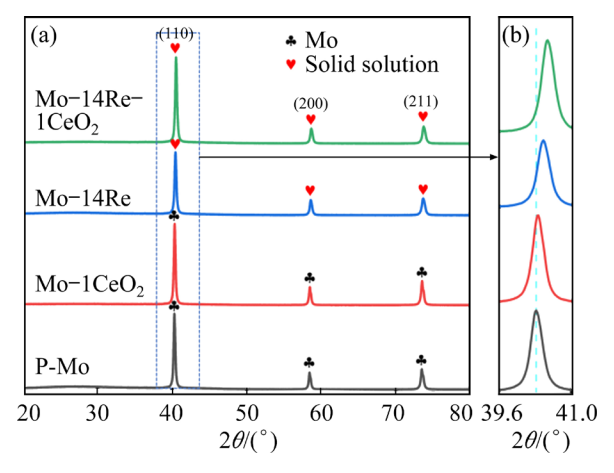


Fig. 2 XRD patterns of various sintered billets: (a) Overview; (b) Enlarged region from 39.6° to 41°

Figure 3 depicts the SEM images of different sintered billets, revealing a noticeable refinement in grain size upon the incorporation of Re and CeO₂. A comparative analysis of grain sizes is also presented in Fig. 4. The grain size of P-Mo is measured to be 13.29 µm, while for the Mo-14Re alloy, it is slightly reduced to be 12.22 µm. Moreover, the addition of CeO2 also results in a remarkable reduction, and the Mo-1CeO2 alloy shows an average grain size of 9.33 µm, suggesting that the CeO₂ impedes grain growth and promotes grain nucleation during the sintering process, thereby reducing the grain size in molybdenum-based alloys [23]. Furthermore, the simultaneous addition of Re and CeO₂ leads to a significant decrease in the grain size, leading to the minimum grain size (8.57 μm) for the Mo-14Re-1CeO₂ alloy, which is about 40.1% smaller than that of P-Mo. Figure 5

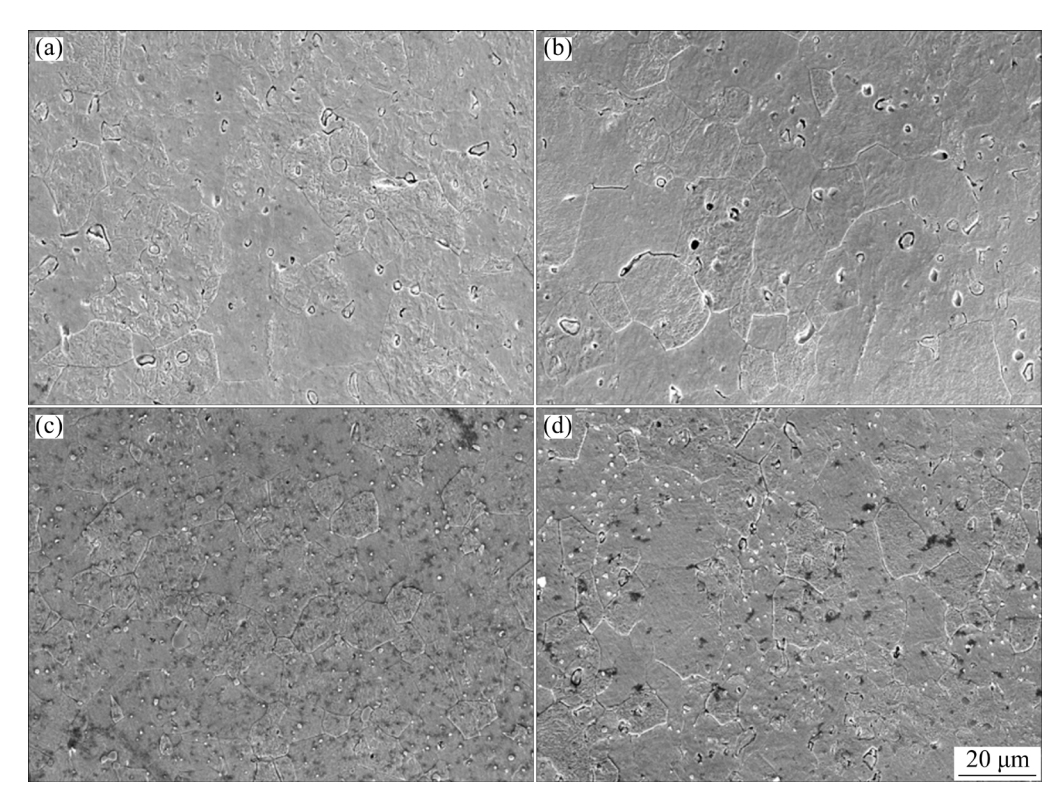


Fig. 3 SEM images of various sintered billets: (a) P-Mo; (b) Mo-14Re; (c) Mo-1CeO₂; (d) Mo-14Re-1CeO₂

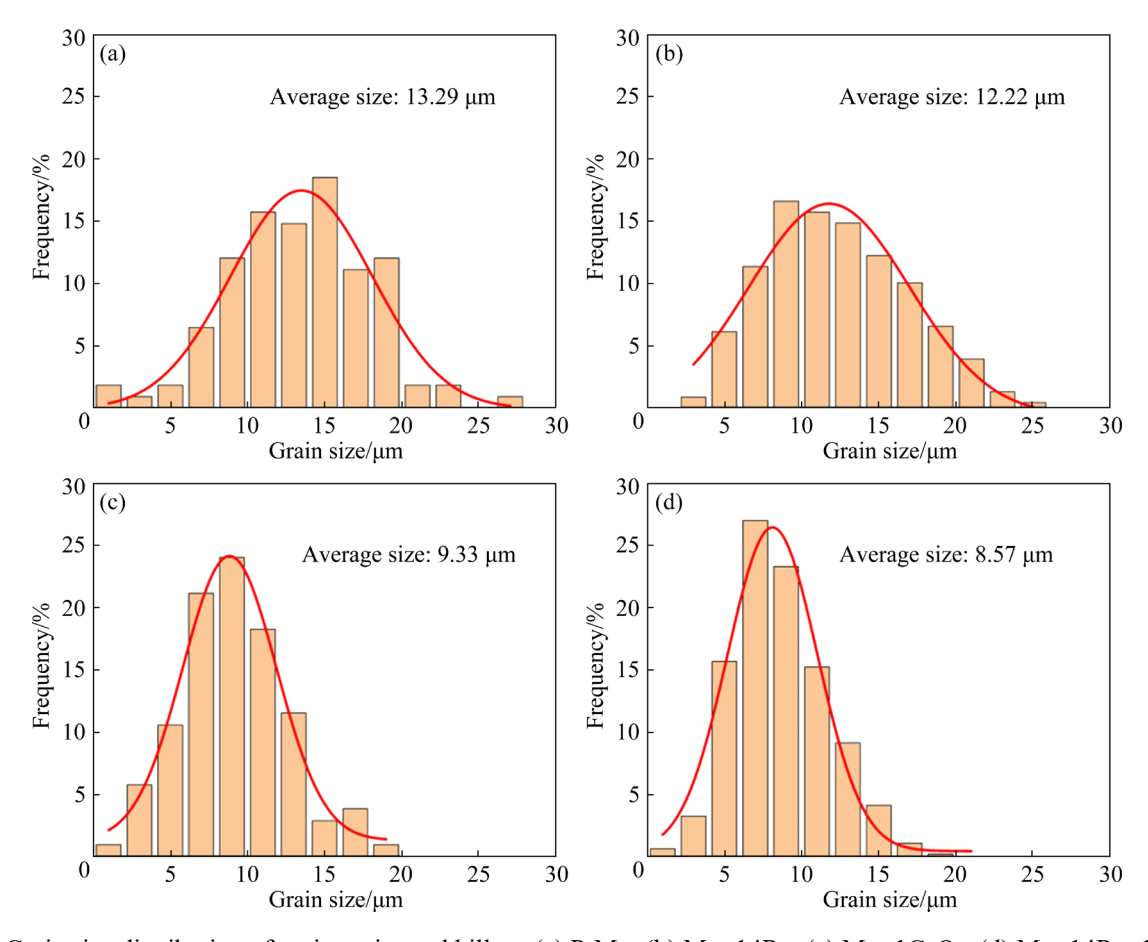


Fig. 4 Grain size distribution of various sintered billets: (a) P-Mo; (b) Mo-14Re; (c) Mo-1CeO₂; (d) Mo-14Re-1CeO₂

illustrates the element distribution within the Mo-14Re-1CeO₂ sample, and the distribution analysis reveals that the Re is uniformly dispersed throughout the matrix. In contrast, the CeO₂ exhibits a diffuse distribution, in the intragranular and intergranular regions. Evidently, the Mo-14Re-1CeO₂ alloy can be expected to present a combined strengthening effect, from the benefits of refined grain size, dispersed phase reinforcement, and solid-solution effect [20].

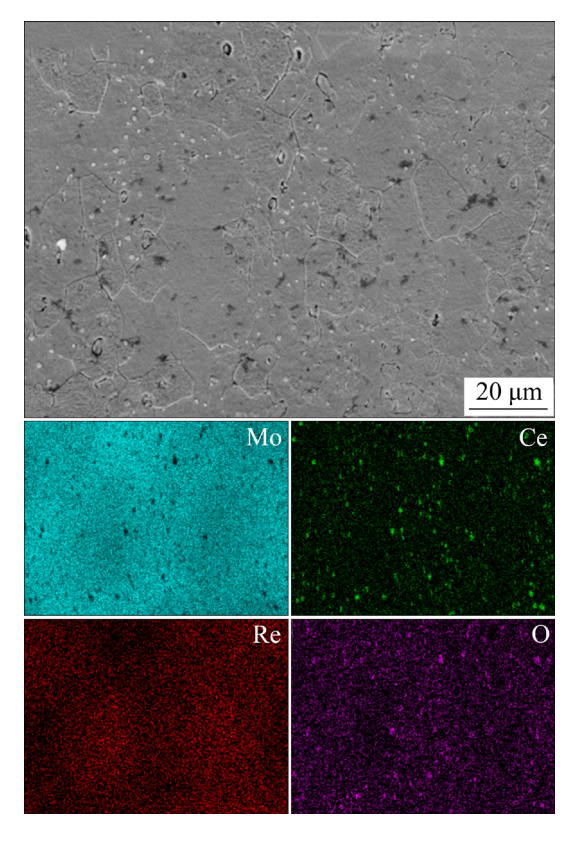


Fig. 5 SEM image and EDS mappings of Mo-14Re-1CeO₂

3.2 Density and mechanical properties

The hardness and relative densities of different billets are detailed in Table 2 and Fig. 6, illustrating a close correlation between the hardness of and densities [24]. The enhancement of densification is intricately linked to the interplay between GB migration and GB diffusion during the final process of sintering [25]. Rapid GB migration can result in the formation of pores within the grains, which are difficult to eliminate. As depicted in Fig. 3, the addition of CeO₂ leads to a significant reduction in surface pores, which should be attributed to the role of CeO₂ as a secondary phase impeding GB migration. Consequently, pores are more effectively

expelled along GBs, resulting in a relatively increased density up to 96.74% for the Mo–1CeO₂ alloy. Similarly, the incorporation of CeO₂ into the Mo–14Re alloy also elevates the relative density to be 96.16%, surpassing that of P-Mo and Mo–14Re. Moreover, the Mo–14Re–1CeO₂ alloy exhibits superior hardness with a value of HV 202.86, higher than that of P-Mo and Mo–14Re.

Table 2 Average grain size, relative densities and hardness of various sintered billets

Campla	Average	Relative	Hardness
Sample	grain size/µm	density/%	(HV)
P-Mo	13.29	92.3	162.9
Mo-14Re	12.22	94.4	177.58
Mo-1CeO ₂	9.33	96.74	191.52
Mo-14Re-1CeO ₂	8.57	96.16	202.86

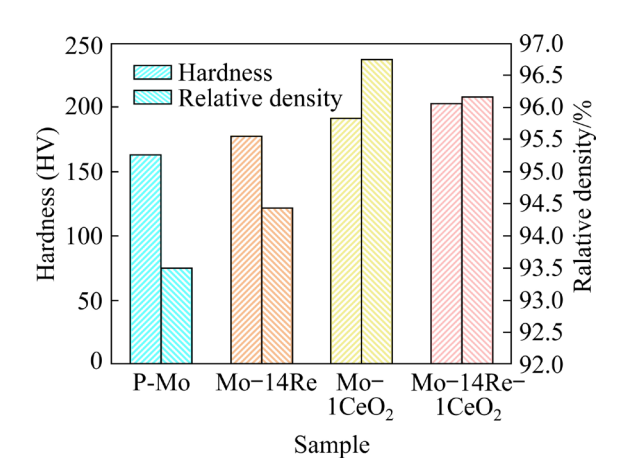


Fig. 6 Comparison of hardness and relative density of various alloys

The tensile strength and elongation of various sintered billets at room temperature (RT) are illustrated in Fig. 7 and Table 3. The addition of Re results in an ultimate tensile strength (UTS) of 543 MPa with a total elongation (TE) of 24.19% for the Mo-14Re alloy, larger than those of pure Mo (453 MPa, and 7.01%), which are primary due to the creation of a molybdenum-rhenium solid solution. When both Re and CeO₂ are introduced to P-Mo, the Mo-14Re-1CeO₂ alloy exhibits a UTS of 657 MPa and a TE of 35.2%, surpassing those of other samples. The inclusion of CeO₂ as a secondary phase introduces a dispersion strengthening effect [14]. Consequently, Mo-14Re-1CeO₂ alloy not only achieves the highest tensile strength but also retains good

plasticity with the largest TE. The combined addition of Re and CeO₂ effectively realizes a synergistic toughening and strengthening effect on the molybdenum alloy.

Figure 8 presents the true compression stress—strain curves of various sintered billets at 1200 °C. Initially, during the elastic deformation stage, stress swiftly increases until it reaches the yield point. Subsequently, in the plastic deformation

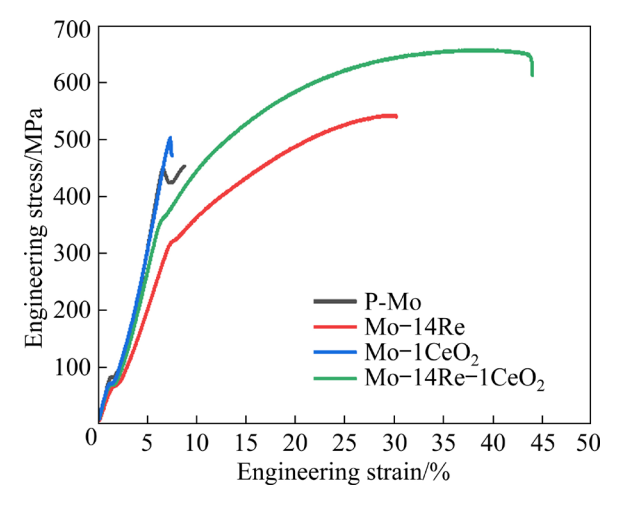


Fig. 7 Tensile engineering stress-strain curves of various billets at RT

Table 3 Total elongation and ultimate tensile strength of various sintered billets

Sample	Total elongation/%	Tensile strength/MPa		
P-Mo	7.01	453		
Mo-14Re	24.19	543		
Mo-1CeO ₂	35.2	657		
Mo-14Re-1CeO ₂	6.02	489		

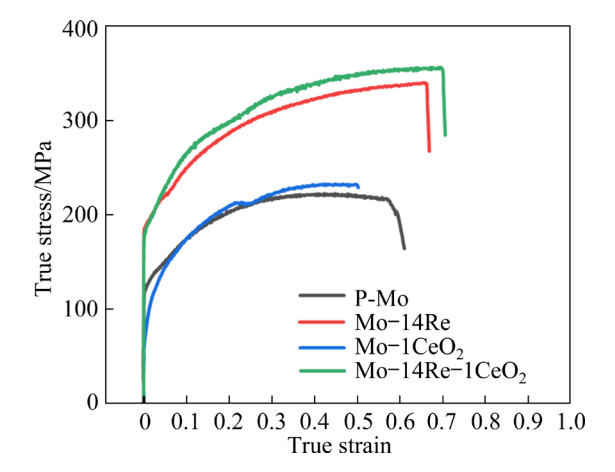


Fig. 8 Representative true compression stress–strain curves of various samples at 1200 °C

stage, the stress continues to escalate with the increment of strain, eventually reaching a plateau and maintaining a steady state. Evidently, the Re plays a crucial role in enhancing the high-temperature strength of Mo alloys, while the CeO₂ only presents a slight promotion. As a result, the Mo–14Re–1CeO₂ achieves the largest UTS of 355 MPa at 1200 °C, about 60.63% higher than that of P-Mo (221 MPa). Besides, it also should be noted the addition of CeO₂ can increase the high-temperature UTS and TE at the same time, which is beneficial for the improvement of high temperature creep resistance ability.

3.3 Fracture behavior

Figure 9 presents morphological characteristics of the tensile fractures on different molybdenum alloys. Fracture surface of P-Mo predominantly exhibits an icosahedral morphology with the majority of distinct intergranular fracturing, signifying a quintessential brittle fracture model, which propagates along the weakest GBs due to strength variations within the alloy. In contrast, the fracture surface of the Mo-14Re alloy exhibits an abundance of river patterns, accompanied with an increased incidence of transgranular fractures, which contributes to the enhanced plasticity relative to P-Mo [26]. Additionally, a small number of dimples are observed at the fracture surface, which corresponds to its relatively good ductility. The Mo-1CeO₂ alloy depicts intergranular fractures with a limited number of transgranular fractures. Notably, fracture surface of Mo-14Re-1CeO₂ alloy is marked by the presence of pronounced dimples and a multitude of river patterns, indicating a significant enhancement in the prevalence of transgranular fractures, which is characteristic of a ductile fracture mechanism.

The EDS analysis of the fracture surface (Fig. 10) reveals the presence of CeO₂ as second-phase particles at the base of elongated dimples. The plastic deformation surrounding the reinforcing particles in Mo-14Re-1CeO₂ alloy is characterized by the presence of tear ridges, which are indicative of significant material flow. This deformation process results in the nucleation of numerous micropores and microcracks, and their further interconnection initiates the coalescence to generate a nucleation site for crack.

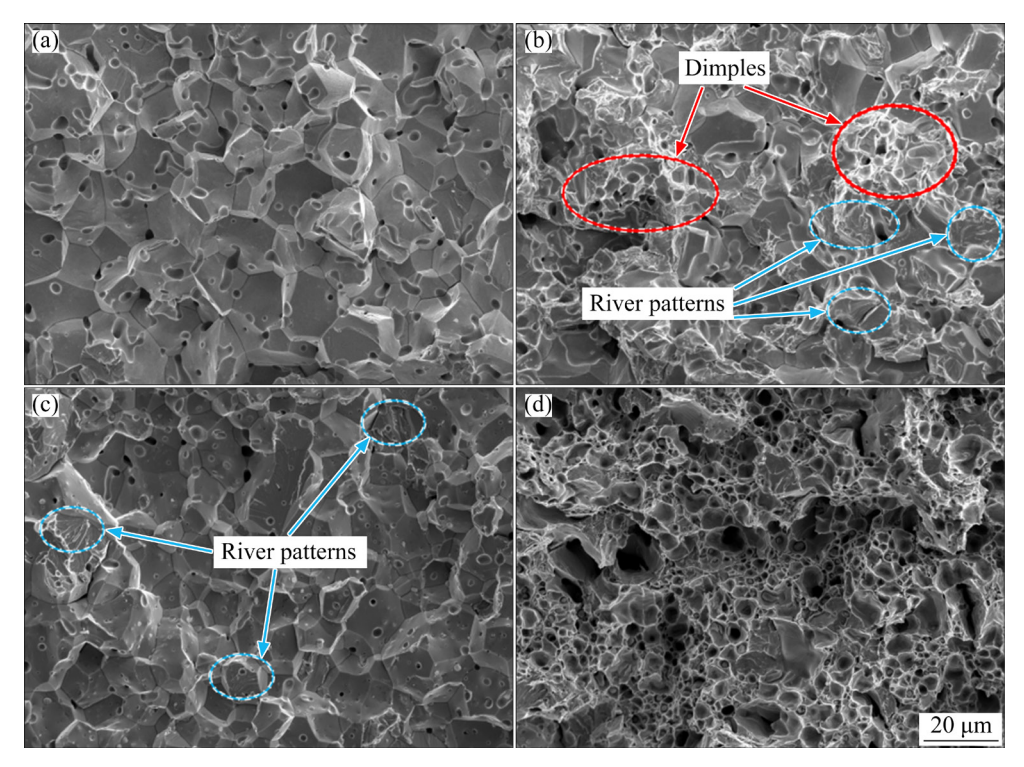


Fig. 9 SEM images showing fracture morphologies of various alloys: (a) P-Mo; (b) Mo-14Re; (c) Mo-1CeO₂; (d) Mo-14Re-1CeO₂

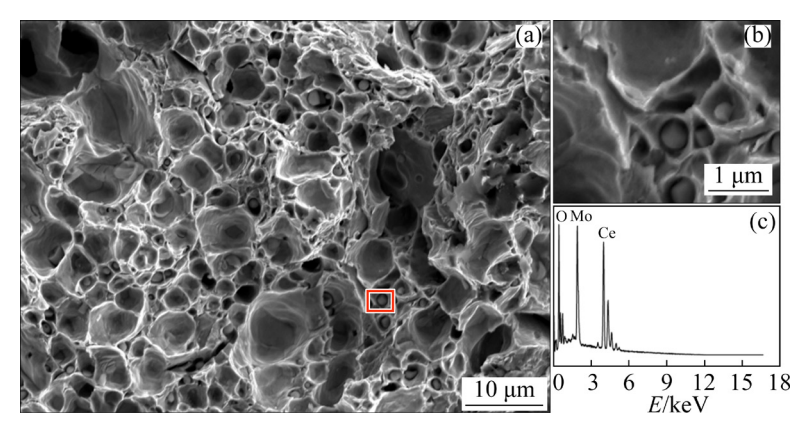


Fig. 10 Fracture morphology (a, b) and EDS analysis results (c) of Mo-14Re-1CeO₂

4 Discussion

The enhancement of mechanical properties is commonly achieved through several key mechanisms, including solid-solution strengthening, fine-grain strengthening, deformation strengthening, and dispersion strengthening of secondary phases [27–29]. In this study, the observed improvements in mechanical performances are predominantly ascribed to three mechanisms: the incorporation of solute atoms into the crystal lattice, the refinement of grain size and the distribution of dispersed

particles.

The increased yield strength $(\Delta \sigma_y)$ of various alloys can be estimated using the specific formula [30,31]:

$$\Delta \sigma_{\rm y} = \Delta \sigma_0 + \Delta \sigma_{\rm SS} + \Delta \sigma_{\rm GB} + \Delta \sigma_{\rm intra} + \Delta \sigma_{\rm inter} \tag{1}$$

where σ_0 represents the intrinsic strength of the Mo lattice and is approximately 360 MPa, σ_{GB} is the additional strength due to the grain refinement; σ_{SS} is the strength increment attributed to the solid-solution effect; σ_{intra} and σ_{inter} present the reinforcing effects of particles that are dispersed within the grains and at GBs. In the case of equiatomic solid

solutions, the contribution from solid-solution strengthening can be integrated into the intrinsic strength term of the yield strength equation. This adjusted intrinsic strength then reflects an average resistance that accounts for the combined effect of all constituent atoms, rather than the resistance offered by a single type of solvent atom [32]. Therefore, the increments of strength attributed to solid-solution strengthening in Mo-14Re and Mo-14Re-1CeO₂ are equivalent. If different atoms are dissolved in a pure element, the crystal structure of the pure element or compound may remain unchanged despite the dissolution, but the lattice parameters are changed due to the solute atoms because of the difference in atomic radii between the two atoms or compounds. Therefore, the solubility of the solute can be calculated using Vegard's law [33]:

$$l(A_{1-C}B_{C}) = (1-C)l_{A} + Cl_{B}$$
(2)

where $l(A_{1-C}B_C)$ is the lattice parameter of the solid solution, l_A is the lattice parameter of the solvent, l_B is the lattice parameter of the solute, and C is the concentration of the solute atoms. According to this law, the atomic concentration of Re is calculated to be 6.64%, which indicates that nearly 86.23% of rhenium atoms are dissolved in the molybdenum matrix.

Obviously, Mo-14Re-1CeO₂ alloy exhibits a relatively fine grain size, which is a result of the inclusion of CeO₂ particles and the creation of the Mo-Re solid solution. The latter not only enhances the thermal stability but also retards grain coarsening. Additionally, the uniform dispersion of CeO₂ particles significantly impedes GB migration and slows down the mass transfer rate. This effect consequently diminishes the diffusion kinetics at GBs [34]. The Hall-Petch relationship provides a quantitative measure of the strengthening effect that arises from the grain size refinement. The specific equation to estimate this fine grain strengthening effect is [35]

$$\Delta \sigma_{\rm GB} = \frac{k}{\sqrt{D}} \tag{3}$$

where k is the Hall-Petch coefficient as a constant (210 MPa· $\sqrt{\mu m}$) for a particular material and D denotes the average grain size. It can be inferred that a reduction in the grain size leads to an increase in the number of grains. According to Table 2, the

strengthening contribution from GBs of Mo-14Re and Mo-14Re-1CeO₂ can be nearly estimated as 57 and 68 MPa, respectively.

It is widely recognized that oxide particles dispersed in a metal matrix can impede GBs motion through a phenomenon known as the Zener pinning effect, which occurs when the second-phase particles intersect and interact with GBs. The migration of GBs, in turn, influences the position and distribution of these oxide particles. During this migration, intergranular CeO₂ particles can detach from the GBs and move into the grain interior [36]. Concurrently, intragranular CeO₂ particles can transform into intergranular oxide particles, generating additional pinning forces. These CeO₂ particles also have the capacity to adsorb impurities, which reduces the concentration of impurities at GBs and consequently strengthens the interface bonding. The intragranular CeO₂ particles act first and impede dislocation movement to form dislocation loops [37,38]. Figure 11 shows the size of CeO₂ particles located intergranularly and intragranularly in Mo-1CeO₂ and Mo-14Re-1CeO₂. Statistical analysis determines that within the Mo-14Re-1CeO₂ alloy, the intragranular CeO₂ particles have an average diameter of 0.85 µm, and the intergranular ones are measured with an average diameter of 0.74 μm. For the Mo-1CeO₂ alloy, the average size of the intragranular CeO₂ particles is 0.97 µm whereas the intergranular CeO₂ particles exhibit an average size of 1.02 µm. It is evident that the incorporation of Re leads to a decrease in particle size of CeO2, in both intergranular and intragranular regions of Mo-14Re-1CeO₂. The primary source of strength enhancement from intragranular particles is attributed to the Orowan mechanism [39]. The corresponding strength contribution can be assessed through the application of the following equation [28,40]:

$$\Delta \sigma_{\text{intra}} = \frac{0.8MGb}{2\pi\sqrt{1 - \nu \lambda_{\text{intra}}}} \ln \left(\frac{\chi}{2b}\right)$$
 (4)

$$\chi = \sqrt{\frac{2}{3}} d_{\text{intra}} \tag{5}$$

where M is the Taylor factor (taken to be 3.06), G is the shear modulus of the Mo matrix (126 GPa), b is the magnitude of Burgers vector (0.273 nm), v is the Poisson's ratio (0.324), λ_{intra} is the average intraparticle spacing and d_{intra} is the average particle size

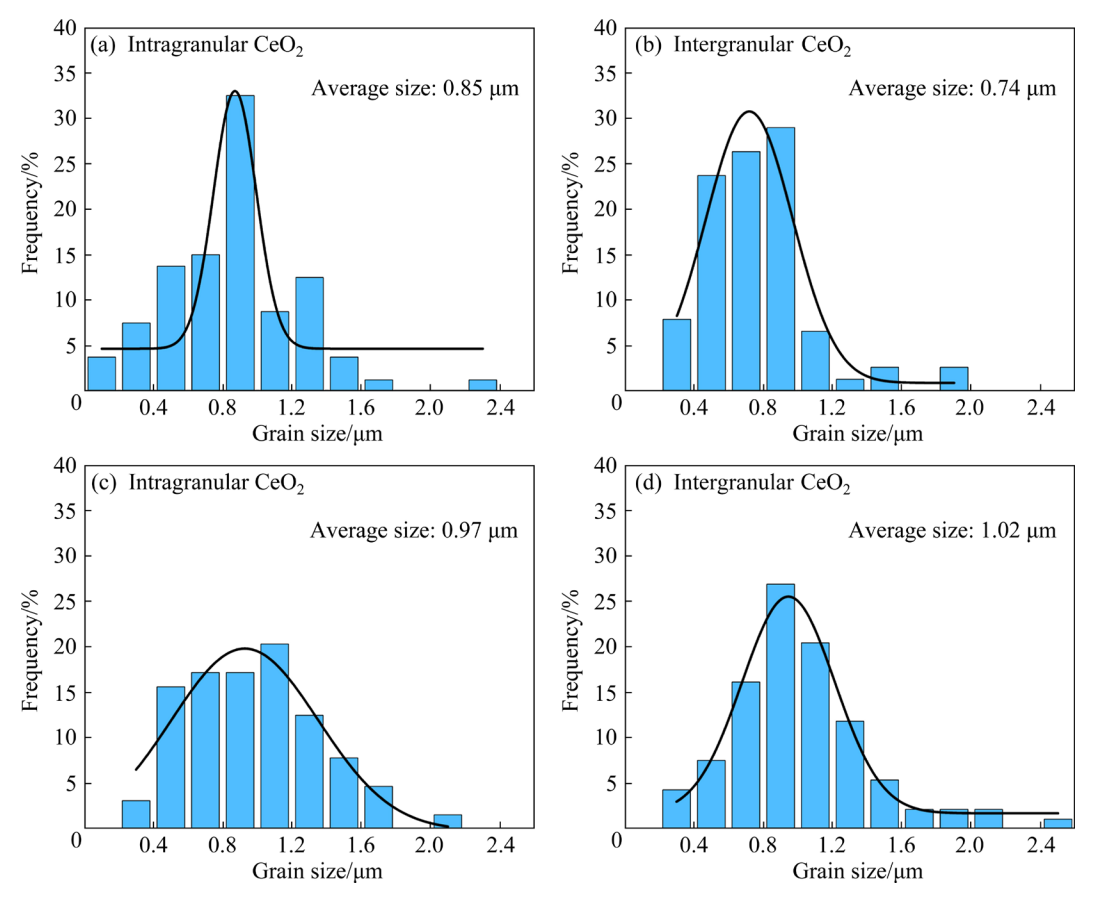


Fig. 11 Particle size distribution of second phases in different alloys: (a, b) Mo-14Re-1CeO₂; (c, d) Mo-1CeO₂

of intragranular CeO₂ particles, as detailed in Table 4. According to the above data, the σ_{intra} can be calculated to be 57 MPa.

The distinct load transfer mechanism for the intergranular particles can be mathematically expressed through the following equations [30,41]:

$$\Delta \sigma_{\text{inter}} = 0.5 f_{\text{inter}} \sigma_0 \tag{6}$$

$$f_{\text{inter}} = 6\pi (d_{\text{inter}}/\lambda_{\text{inter}})^3 \tag{7}$$

where f_{inter} is the volume fraction of intergranular particles, λ_{inter} is the average inter-particle spacing and d_{inter} is the average particle size of intergranular CeO₂ particles. From the data presented in Table 4, the σ_{inter} of Mo-14Re-1CeO₂ can be estimated to be

Table 4 Statistical results on intragranular and intergranular particles of Mo-14Re-1CeO₂

Parameter	
Average grain size, D/μm	8.57
Average intragranular particle size, $d_{intra}/\mu m$	
Average intragranular particle spacing, $\lambda_{intra}/\mu m$	
Average intergranular particle size, $d_{inter}/\mu m$	
Average intergranular particle spacing, $\lambda_{inter}/\mu m$	

about 20 MPa.

Figure 12 illustrates the enhancement resulting from various strengthening effects, as calculated based on the established formulas. The Mo-14Re-1CeO₂ alloy exhibits an approximate 88 MPa increase in yield strength over the Mo-14Re alloy, which agrees will with the experimental data (Fig. 7).

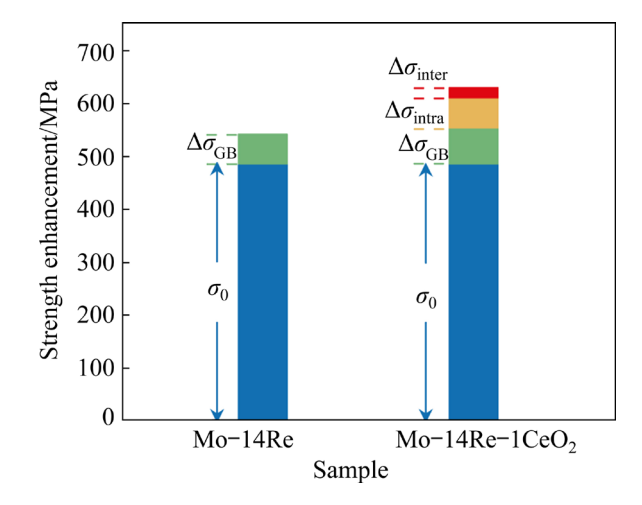


Fig. 12 Calculated enhancement of tensile strength induced by different strengthening effects

Typically, in the process of plastic deformation at room temperature, a multitude of dislocations within molybdenum tend to slip towards the GBs, leading to high stress concentrations at GBs [34]. The occurrence of this phenomenon is a principal contributor to the embrittlement observed in molybdenum. As shown in Fig. 13, CeO₂ particles are observed using TEM. On one hand, the CeO₂ particles within the Mo-14Re-1CeO₂ alloy impede dislocation motion, thereby increasing dislocation interactions, as illustrated in Figs. 13(a, b). The dislocations cannot cut through the CeO₂ particles and thus are pinned up around them (Figs. 13(e, f)). On the other hand, the presence of CeO₂ particles also restricts the GB migration, leading to a reduction in the average grain size (Figs. 3 and 4), thereby achieving grain refinement strengthening. Figure 13(d) reveals interface structure between the Mo-14Re solid solution and CeO₂. The interplanar spacing within the Mo matrix is 0.218 nm, aligning closely with the characteristic spacing of the Mo (110) plane, while that of CeO₂ is 0.228 nm. The presence of coherent interfaces without pores and microcracks facilitates enhanced interfacial bonding, which contributes to the superior mechanical properties [26,42]. Additionally, as strain increases, dislocations rearrange to form the substructure boundaries, thereby lowering the free energy of the system.

As indicated in Table 2, Mo-14Re-1CeO₂ alloy exhibits a smaller average grain size compared to the other three alloys. Consequently, under an equivalent external force, increased grains are oriented in a direction conductive to dislocation slip, engaging more grains in the slip process [43]. The slip is then distributed across a larger number of grains, promoting more uniform deformation and reducing stress concentration. This reduction in stress concentration minimizes the likelihood of crack initiation and propagation during the plastic

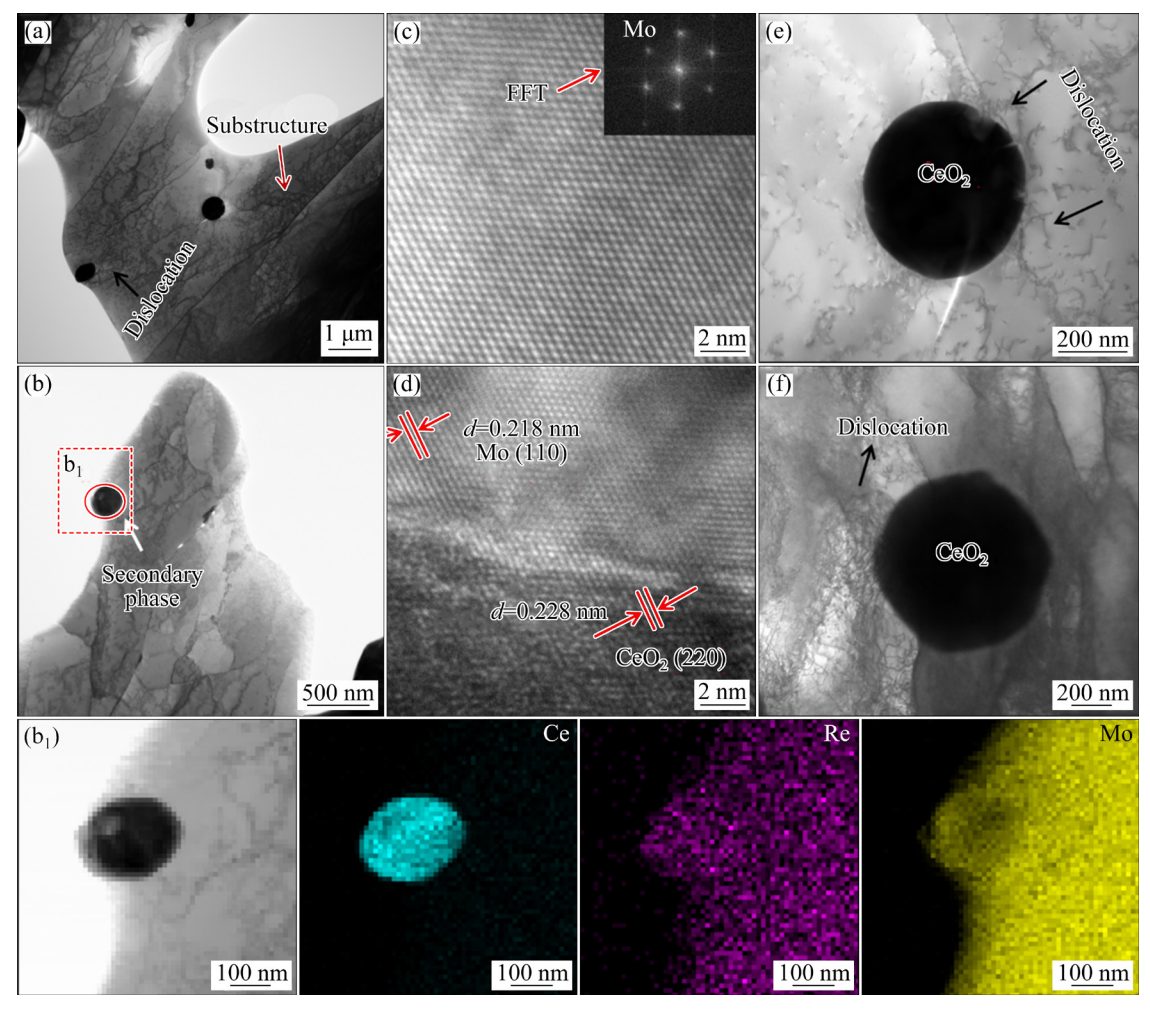


Fig. 13 HRTEM images of Mo-14Re-1CeO₂: (a) Deformation-induced substructures; (b, d) Interface structure between matrix and second phase; (c) High-resolution TEM image and Fourier transform of matrix; (e, f) Secondary phases hinding dislocations

deformation. Secondly, the grain refinement increases the total grain boundary area, which in turn lowers the abundance of impurity elements at GBs [44]. This decrease in impurity concentration enhances the GB bonding strength, making it less probable for cracks to nucleate. Thirdly, the increased GB network following grain refinement makes the path for crack propagation more convoluted [45]. As a result, the Mo alloy is required to absorb greater energy to fracture, which translates to a higher energy demand during the deformation process. Therefore, the Mo-14Re-1CeO₂ alloy is capable of achieving larger plastic deformation and energy absorption, thereby enhancing the overall plasticity.

Figure 14 shows tensile fracture morphologies of Mo-14Re-1CeO₂. Firstly, the fracture surface has many tear ridges formed by plastic fracture, indicating that a portion of molybdenum grains are plastically deformed during crack extension. This implies that the alloy can consume more energy before fracture. Additionally, the observation of river patterns in Fig. 14(b) signifies intragranular fracture, which also requires increased energy for fracture. Finally, Fig. 14(a) demonstrates that

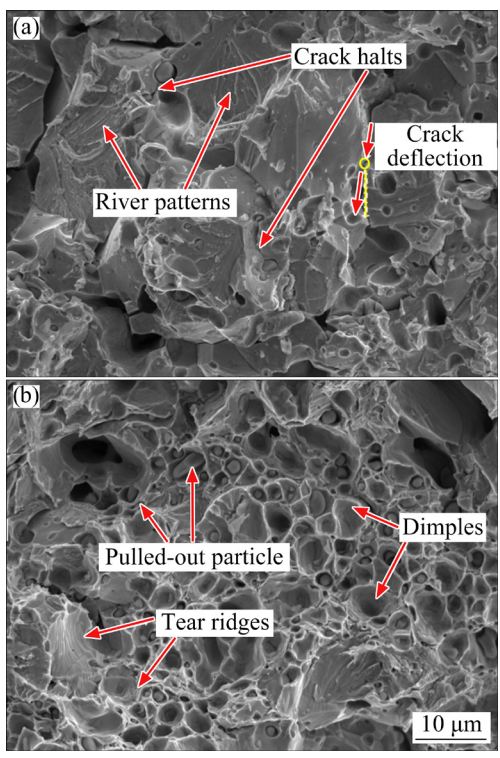


Fig. 14 Tensile fracture surface morphologies of Mo–14Re–1CeO₂: (a) Tearing ridges and extracted second phase particles; (b) Second phase particles inhibiting crack propagation and inducing crack deflection

during crack propagation, second-phase particles are partially pulled out and can either impede crack extension or cause cracks to deflect, leading to a more tortuous crack path [46,47]. This complexity increases the surface energy associated with crack propagation and acts to inhibit fracture initiation. These characteristics collectively contribute to the enhanced plasticity of the molybdenum alloy [48].

5 Conclusions

- (1) The addition of Re and CeO₂ can enhance the tensile strength of the Mo matrix at RT.
- (2) The Mo-14Re-1CeO₂ exhibits the highest UTS of 657 MPa with the largest TE of 35.2% at RT, much higher than those of pure Mo (453 MPa, and 7.01%). Moreover, it also presents the largest high-temperature (1200 °C) compression strength of 355 MPa, about 134 MPa higher than that of pure Mo.
- (3) A coherent interface is formed between CeO₂ and the Mo-14Re matrix with CeO₂ particles uniformly distributed in both intergranular and intragranular regions.
- (4) The mechanical property improvement is predominantly attributed to the formation of Mo–Re solid solution, grain refinement and dispersion strengthening effect of CeO₂ particles.

CRediT authorship contribution statement

Meng-yao ZHANG: Conceptualization, Data curation, Formal analysis, Methodology, Writing – Original draft; Shuai MA: Methodology, Conceptualization, Supervision; Xin LI: Methodology, Supervision; Ye GAO: Validation, Data curation; Zhuang-zhi WU: Supervision, Formal analysis, Writing – Review & editing; De-zhi WANG: Supervision, Writing – Review & editing.

Declaration of competing interest

The authors declare that they have no known competing financial interests or personal relationships that could have appeared to influence the work reported in this paper.

Acknowledgments

This work was supported by the National Key R&D Program of China (No. 2022YFB3705402).

References

- DUAN Bo-hua, ZHANG Zhao, WANG De-zhi, ZHOU Tao. Microwave sintering of Mo nanopowder and its densification behavior [J]. Transactions of Nonferrous Metals Society of China, 2019, 29: 1705–1713.
- [2] MAJUMDAR S, RAVEENDRA S, SAMAJDAR I, BHARGAVA P, SHARMA I. Densification and grain growth during isothermal sintering of Mo and mechanically alloyed Mo-TZM [J]. Acta Materialia, 2009, 57: 4158-4168.
- [3] YOON Y H, LEE S Y, GWON J G, CHO H J, KIM Y H, LEE W H. Photocatalytic performance of highly transparent and mesoporous molybdenum-doped titania films fabricated by templating cellulose nanocrystals [J]. Ceramics International, 2018, 44: 16647–16653.
- [4] HIRAOKA Y, OGUSU T, YOSHIZAWA N. Decrease of yield strength in molybdenum by adding small amounts of Group VIII elements [J]. Journal of Alloys and Compounds, 2004, 381: 192–196.
- [5] SUN Tie-long, XU Liu-jie, WEI Shi-zhong, PAN Kunming, LI Wu-hui, ZHOU Yu-cheng, HUANG Zhi-min. Microstructure and compression properties of fine Al₂O₃ particles dispersion strengthened molybdenum alloy [J]. Transactions of Nonferrous Metals Society of China, 2020, 30: 3307–3321.
- [6] WANG De-zhi, JI Yao-xin, WU Zhuang-zhi. Effects of crossrolling on texture mechanical properties and anisotropy of pure Mo plates [J]. Transactions of Nonferrous Metals Society of China, 2020, 30: 2170–2176.
- [7] WANG Miao, YANG Shuang-ping, LIU Hai-jun, XIN Yang, WANG Li-dong. Research progress and prospect of strengthening and toughening of molybdenum alloys [J]. Rare Metal Materials and Engineering, 2021, 50: 3158-3168.
- [8] ZHANG Yu-heng, MA En, SUN Jun, HAN Wei-zhong. Unveiling the intrinsic rhenium effect in tungsten [J]. Acta Materialia, 2024 264: 119586.
- [9] LEICHTFRIED G, SCHNEIBEL JH, HEILMAIER M. Ductility and impact resistance of powder-metallurgical molybdenum-rhenium alloys [J]. Metallurgical and Materials Transactions A, 2006, 37: 2955–2961.
- [10] LU Ke-long, LUO Bin, WANG Guang-da, HUANG Hong-tao, CHEN Fu-ge. High-temperature mechanical properties and dynamic recrystallization of Mo-14Re alloy [J]. Materials Characterization, 2024, 208: 113617.
- [11] HUANG Hong-tao, WANG Wei-jun, ZHONG Wu-ye, ZHENG Jian-ping, ZHAO Shou-zhi. Research progress on application of Mo-Re alloy in space nuclear power [J]. Atomic Energy Science and Technology, 2020, 54: 505-511. (in Chinese)
- [12] LAN Xin, LI Zhi-bo, ZHANG He, ZHANG Guo-hua. Effect of rare earth oxide doping on microstructure and mechanical property of Mo-30W solid solution alloy [J]. International Journal of Refractory Metals and Hard Materials, 2023, 110: 106014.
- [13] WU Zhuang-zhi, ZHAO Na, LU Yao. Influence of the shape

- and size of the second phase on the mechanical properties of sintered Mo-Y₂O₃ alloy [J]. Transactions of Nonferrous Metals Society of China, 2022, 32: 1926–1934.
- [14] WU Zhuang-zhi, LIU Xin, WANG De-zhi. Synthesis of high-performance Mo-La₂O₃ powder by hydrogen reduction of MoO₂ originated from a self-reduction strategy [J]. Materials Research Express, 2019, 6: 126586.
- [15] ZHANG He, LI Zhi-bo, DENG Xiao-chun, CHEN Ben, ZHANG Guo-hua, CHOU K C. Effects of various rare earth oxides on morphology and size of oxide dispersion strengthening (ODS)-W and ODS-Mo alloy powders [J]. Transactions of Nonferrous Metals Society of China, 2022, 32: 2665–2680.
- [16] WANG Lin, SUN Jun, LIU Gang, SUN Yuan-jun, ZHANG Guo-jun. Influences of annealing temperature on microstructure and mechanical properties of Mo-La₂O₃ [J]. International Journal of Refractory Metals and Hard Materials, 2011, 29: 522-527.
- [17] MUELLER A J, BIANCO R, BUCKMAN R W. Evaluation of oxide dispersion strengthened (ODS) molybdenum and molybdenum-rhenium alloys [J]. International Journal of Refractory Metals and Hard Materials, 2000, 18: 205–211.
- [18] XING Hai-rui, HU Ping, HE Chao-jun, ZHANG Xiang-yang, HAN Jia-yu, YANG Fan, BAI Run, ZHANG Wen, WANG Kuai-she, VOLINSKY A. Research Progress in dispersion strengthened molybdenum alloys design of highperformance molybdenum alloys via doping metal oxide and carbide strengthing: A review [J]. Journal of Materials Science & Technology, 2023, 160: 161–180.
- [19] LIU Ren-zhi, AN Geng, YANG Qin-li, ZHUANG Fei, WANG Yin-ting, CUI Yu-qing, WANG Na, CAO Wei-cheng. Microstructures and mechanical properties of Mo-Re-La alloy [J]. Powder Metallurgy Technology, 2018, 36: 429-432.
- [20] WANG De-zhi, HE Dong-yang, LI Kai, WU Zhuang-zhi. Preparation and in-situ strengthening mechanisms of Mo composites with the addition of WC [J]. Materials Science and Engineering A, 2022, 848: 143478.
- [21] ZHANG Cheng, WANG Pei, LIU Chang-yong, PRASHANTH K G, CHEN Zhang-wei. A novel crack-free Ti-modified Mo alloy designed for laser powder bed fusion [J]. Journal of Alloys and Compounds, 2022, 910: 164802.
- [22] WANG De-zhi, XING Ning-yuan, LI Kai, GAO Ye, LU Yan-zhen, WU Zhuang-zhi. Effect of titanium-based additives on the strengthening of tungsten composites [J]. International Journal of Refractory Metals and Hard Materials, 2024, 121: 106686.
- [23] CHENG Hui-zhao, LIU Pin-pin, FAN Jing-lian, TIAN Jia-min, LI Peng-fei. Effect of Y₂O₃ on the sintering performance and microstructure of ultrafine Mo composite powder [J]. Powder Metallurgy Science and Technology, 2011, 16: 355–360.
- [24] LI Mian-mian, ZU Ming, YU Yang, ZHANG Wen-cong. Elevated temperature tensile behavior and microstructure evolution of liquid phase sintered 90W-7Ni-3Fe alloy [J]. Journal of Alloys and Compounds, 2019, 802: 528-534.
- [25] ZHOU Mao, HUANG Zhang-yi, QI Jian-qi, WEI Nian, WU Di, ZHANG Qing-hua, WANG Shan-shan, FENG Zhao, LU Tie-cheng. Densification and grain growth of Gd₂Zr₂O₇

- nanoceramics during pressureless sintering [J]. Journal of the European Ceramic Society, 2017, 37: 1059–1065.
- [26] LI Kai, GAO Ye, MA Shuai, LU Yan-zhen, WU Zhuang-zhi, WANG De-zhi. Enhanced mechanical properties originating from the B doping over Mo-Y₂O₃ composites [J]. International Journal of Refractory Metals and Hard Materials, 2024, 119: 106561.
- [27] MILLER W S, HUMPHREYS F J. Strengthening mechanisms in particulate metal matrix composites [J]. Scripta Metallurgica et Materialia, 1991, 25: 33–38.
- [28] KAMIKAWA N, SATO K, MIYAMOTO G, MURAYAMA M, SEKIDO N, TSUZAKI K, FURUHARA T. Stress-strain behavior of ferrite and bainite with nano-precipitation in low carbon steels [J]. Acta Materialia, 2015, 83: 383-396.
- [29] HE Jun-yang, WANG Hui, HUANG Hai-long, XU Xian-dong, CHEN Ming-wei, WU Yuan, LIU Xiong-jun, NIEH T G, AN Ke, LU Zhao-ping. A precipitation-hardened high-entropy alloy with outstanding tensile properties [J]. Acta Materialia, 2016, 102: 187–196.
- [30] LIU Gang, ZHANG Gun-jun, JIANG Feng, DING Xiangdong, SUN Yuan-jun, SUN Jun, MA E. Nanostructured high-strength molybdenum alloys with unprecedented tensile ductility [J]. Nature Materials, 2013, 12: 344–350.
- [31] JING Kai, LIU Rui, XIE Zhuo-ming, WANG Huan, LI Gang, WU Xue-bang. Excellent high-temperature strength and ductility of the ZrC nanoparticles dispersed molybdenum [J]. Acta Materialia, 2022, 227: 117725.
- [32] LI Heng, ZONG Hong-xiang, LI Su-zhi, JIN Shen-bao, CHEN Yan, CABRAL M J, CHEN Bing, HUANG qian-wei, REN Yang, YU Kai-yuan, HAN Shuang, DING Xiang-dong, SHA Gang, LIAN Jian-she, LIAO Xiao-zhou, MA En, SUN Jun. Uniting tensile ductility with ultrahigh strength via composition undulation [J]. Nature, 2022, 604: 273–279.
- [33] DENTON A R, AXHCROFT N W. Vegard's law [J]. Physical Review A, 1991, 43: 3161–3164.
- [34] LI Peng-fei, FAN Jing-lian, HAN Yong, ZHANG Man, TIAN Jia-min. Study on the strengthening and toughening mechanism and interface bonding of W-ZrC material [J]. Rare Metal Materials and Engineering, 2019, 48: 751-757.
- [35] GAN Jian-ning, GONG Qian-ming, JIANG Yan-qi, CHEN Hao, HUANG Yi-lun, DU Kai, LI Yu-yao, ZHAO Ming, LIN Feng, ZUANG Da-ming. Microstructure and high-temperature mechanical properties of second-phase enhanced Mo-La₂O₃-ZrC alloys post-treated by cross rolling [J]. Journal of Alloys and Compounds, 2019, 796: 167–175.
- [36] WANG Yi-ming, AKTAA J. Microstructure and texture in W and W-1wt.%La₂O₃ processed by high-pressure torsion [J]. Scripta Materialia, 2017, 139: 22–25.
- [37] CHEN Peng-qi, XU Xian, WEI Bang-zheng, CHEN Jia-yu, QIN Yong-qiang, CHENG Ji-gui. Enhanced mechanical properties and interface structure characterization of W-La₂O₃ alloy designed by an innovative combustion-based approach [J]. Nuclear Engineering and Technology, 2021, 53: 1593-1601.

- [38] CHENG Peng-ming, ZHANG Gon-jun, ZHANG Jin-yu, LIU Gang, SUN Jun. Coupling effect of intergranular and intragranular particles on ductile fracture of Mo–La₂O₃ alloys [J]. Materials Science and Engineering A, 2015, 640: 320–329.
- [39] GUAN Kai, ZHANG Jing-huai, YANG Qiang, LI Bai-shun, WU Rui-zhi, MENG Jian. Effects of trace Ca addition on microstructure and mechanical properties of as-cast Mg-Sm-Gd-based alloy [J]. Transactions of Nonferrous Metals Society of China, 2023, 33: 46-58.
- [40] SANATY-ZADEH A. Comparison between current models for the strength of particulate-reinforced metal matrix nanocomposites with emphasis on consideration of Hall-Petch effect [J]. Materials Science and Engineering A, 2012. 531: 112–118.
- [41] LU Tian-xing, CHEN Cun-guang, LI Pei, ZHANG Chenzeng, HAN Wei-hao, ZHOU Yang, CHALLAPALLI S, GUO Zhi-meng. Enhanced mechanical and electrical properties of in situ synthesized nano-tungsten dispersion-strengthened copper alloy [J]. Materials Science and Engineering A, 2021, 799: 140161.
- [42] LI Kai, HE Dong-yang, LIU Hai-lang, WU Zhuang-zhi, WANG De-zhi. In situ phase interface engineering of MoLa alloys for enhanced strength [J]. International Journal of Refractory Metals and Hard Materials, 2023, 110: 106050.
- [43] WANG De-zhi, LU Yao, LIU Xin-li, DUAN Bo-hua, WU Zhuang-zhi. Boosted mechanical properties of sintered MoLa alloys with ultrafine-grains by the nanostructuring of secondary phase [J]. Materials Science and Engineering A, 2020, 798: 140270.
- [44] LI Zhi-bo, ZHANG He, ZHANG Guo-hua, CHOU K C. Superior strength-ductility synergy in a novel tailored Zr-based particle-strengthened medium W content alloys [J]. Composites Part B: Engineering, 2022, 236: 109817.
- [45] YANG Jun-jun, CHEN Gang, CHEN Zheng, MU Xiao-dong, YU Ying, ZHANG Lin, LI Xing-yu, QU Xuan-hui. Effects of doping route on microstructure and mechanical properties of W-1.0wt.%La₂O₃ alloys [J]. Transactions of Nonferrous Metals Society of China, 2020, 30: 3296-3306.
- [46] HE Dong-yang, LIU Hai-lang, WU Zhuang-zhi, WANG De-zhi. Collaborative improvement of strength and ductility over Mo composites enabled by WC and La₂O₃ [J]. International Journal of Refractory Metals and Hard Materials, 2023, 117: 106419.
- [47] QIN Yong-qiang, ZHUANG Yi, LUO Lai-ma, ZHANG Yi-fan, WU Yu-cheng. Effect of alloying element Zr on microstructure and properties of Cu-Y₂O₃ composites [J]. Transactions of Nonferrous Metals Society of China, 2023, 33: 3418-3426.
- [48] HU Bo-liang, HAN Jia-yu, GE Song-wei, HUA Xing-jiang, LI Shi-lei, XING Hai-rui, WANG Kuai-she. Secondary phases strengthening-toughening effects in the Mo-TiC-La₂O₃ alloys [J]. Materials Science and Engineering A, 2022, 831: 142271.

铼及二氧化铈复合强化钼合金的力学性能

张梦瑶¹, 马 m^1 , 李 a_1 , 高 a_2 , 高 a_3 , 吴壮志^{1,2}, 王德志^{1,2}

- 1. 中南大学 材料科学与工程学院,长沙 410083;
- 2. 中南大学 粉末冶金国家重点试验室,长沙 410083

摘 要:为了提高钼合金在常温及高温条件下的力学性能,采用粉末冶金方法制备 $Mo-14Re-1CeO_2$ 合金,并探 究其微观结构和力学性能。结果表明, $Mo-14Re-1CeO_2$ 的极限抗拉强度达到 657 MPa,总伸长率为 35.2%,明显 高于纯钼(453 MPa、7.01%)。另外, $Mo-14Re-1CeO_2$ 在高温(1200 $^{\circ}$ C)下的压缩强度达到 355 MPa,同样高于纯钼 (221 MPa)。 CeO_2 与 Mo-14Re 基体间形成共格界面,且 CeO_2 颗粒均匀分布于晶界和晶内。该合金力学性能的提升主要归因于 Mo-Re 固溶体的形成、晶粒细化以及 CeO_2 颗粒的弥散强化效应。

关键词: 钼铼合金; CeO2; 复合强化; 力学性能

(Edited by Bing YANG)